OPEN ACCESS

University of BRISTOL

Peer reviewed version

University of Bristol - Explore Bristol Research
General rights

PAPER

Growth and electronic structure of 2D hexagonal nanosheets on a corrugated rectangular substrate

View the article online for updates and enhancements.

IOP ebooks™

Bringing you innovative digital publishing with leading voices to create your essential collection of books in STEM research.

Start exploring the collection - download the first chapter of every title for free.

Growth and electronic structure of 2D hexagonal nanosheets on a corrugated rectangular substrate

Simona Achilli[1,4] , **Emanuele Cavaliere**[2]**, Thanh Hai Nguyen**[3]**,**
Mattia Cattelan[3] **and Stefano Agnoli**[3]

[1] Department of Physics, European Theoretical Spectroscopy Facility (ETSF), University of Milano, Via Celoria 16, 20133 Milano, Italy
[2] Interdisciplinary Laboratories for Advanced Materials Physics (iLAMP) and Mathematics and Physics Department, Catholic University, via dei Musei 41, 25121 Brescia, Italy
[3] Department of Chemical Sciences, University of Padova, Via Marzolo 1, 35131 Padova, Italy

E-mail: simona.achilli@unimi.it and stefano.agnoli@unipd.it

CrossMark

Abstract

Graphene and h-BN are grown by chemical vapor deposition in ultra high vacuum conditions on the Pt(110) surface. Scanning tunneling microscopy measurements and low-energy electron diffraction data indicate that graphene forms a variety of differently oriented incommensurate domains although with a strong preference to align its $[11\bar{2}0]$ direction with the $[00\bar{1}]$ direction of Pt. Meanwhile, h-BN exhibits a $c(8 \times 10)$ commensurate superstructure, which presents a high level of defectivity that implies local variation of the periodicity (i.e. mixed $c(8 \times 10)$ and $c(8 \times 12)$ patches) and the introduction of local defects. The combination of advanced photoemission spectroscopy data (angle-resolved photoemission spectroscopy from the valence band) and *ab initio* calculations indicates that both 2D materials interact weakly with the substrate: graphene exhibits neutral doping and is morphologically flat, even if it nucleates on the relatively highly corrugated rectangular (110) surface. In the case of h-BN, the interaction is slightly stronger and is characterized by a small electron transfer from surface Pt atoms to nitrogen atoms. The (110) termination of Pt is therefore a quite interesting surface for the growth of 2D materials because given its low symmetry, it may favor the growth of selectively oriented domains but does not affect their pristine electronic properties.

Supplementary material for this article is available online

Keywords: h-BN, graphene, Pt(110), DFT, PES, STM, LEED

(Some figures may appear in colour only in the online journal)

Introduction

The technological implementation of 2D materials in practical applications is often based on the possibility to tune their properties by means of functionalization and interaction with a substrate [1–7]. The comprehension of the structural properties and growth mechanism of 2D materials on metal substrates represents a stepping stone for the development of

novel devices [8, 9]. So far, most investigations have focused on the growth of graphene and another 2D material, such as h-BN [10], or transition metal chalcogenides [11] on flat hexagonal substrates. However, little is known in the literature about the preparation of 2D nanosheets on highly anisotropic surfaces with a different symmetry and roughness at the nanoscale. Single layers of graphene and h-BN represent some of the most interesting 2D atomic crystals since they are quite versatile and present complementary properties: the former is a semimetal with exceptional electronic mobility

---

while the latter is an excellent insulator. Nonetheless, their combination according to a rational design can lead to hybrid materials or devices with innovative properties [12, 13]. Quite interestingly, if supported on transition metals, these materials can be used as templates for the growth of other nano-objects, such as nanoparticles or functional molecules, since they allow controlling the spatial organization at the nanoscale or may enable a precise modulation of the interaction with metal substrates [14]. In the present work, we studied the growth on the Pt(110) surface and then investigated the structural properties of these two archetypal sp^2 hybridized nanosheets by combining spectroscopic (photoemission spectroscopy), diffraction (low-energy electron diffraction), and microscopic techniques (scanning tunneling spectroscopy) together with state-of-the-art density functional theory (DFT) calculations.

The Pt(110) surface is chemically inert but very intriguing from the structural point of view. As a matter of fact, it reconstructs under ultra high vacuum (UHV) conditions to form a (1×2) 'missing row' superstructure that is highly anisotropic, being constituted by linear chains of atoms along the $[1\bar{1}0]$ direction separated by missing rows. Moreover, at the mesoscale it is characterized by a 'fish scale' morphology and a buckled structure where highly stepped areas, which are a micrometer long and aligned with the $[1\bar{1}0]$ direction, are separated by regions of relatively large terraces over a length scale of about 150 nm.

The growth of graphene on several Pt substrates, either single crystals [15, 16] or polycrystalline foils [17, 18], has been thoroughly studied in recent years. In order to pave the way toward technological applications, several procedures have been developed for removing the graphene layer from the substrate in a nondestructive way so that the same metal foil can be used several times [19, 20], thus sparking huge interest in the study of the graphene/Pt system. In the case of the Pt(111) surface, several studies under UHV conditions have obtained a rather clear understanding of the growth mode and electronic properties [21]. It is well know that the interaction between Pt and graphene is very weak, as suggested by the large graphene–metal substrate bond distance (3.1 Å) and by the electronic properties of supported graphene, which are almost identical to the isolated freestanding material [22, 23]. From the structural point of view, the scarce interaction between Pt and graphene and the large lattice mismatch (11%) leads to the formation of several different epitaxial structures (Moiré patterns), where the graphene overlayer is fully relaxed and adopts several different orientations with respect to the substrate [22, 24]. However, quite recently this view has been challenged by a study combining angle-resolved photoemission spectroscopy (ARPES) and first-principle calculations, which highlights a strong effect of the Pt substrate on the electronic properties of graphene, leading to a substantial *p*-doping (0.44 eV) and the formation of discontinuities in energy versus momentum dispersion where the band of the substrate and overlayer cross each other [25].

Regarding the growth of graphene on surfaces with symmetry other than hexagonal, such as Ni(110), Fe(110), and Cu(110), scanning tunneling microscopy (STM) investigations mostly indicate that the formation of uniaxially corrugated graphene layers commensurate with the substrate. The morphology observed for graphene on Ni(110) [26] and Fe(110) [27] is the product of the strong interaction between the C atoms and these transition metals and the different symmetry between the support and overlayer: graphene is hexagonal while the Ni(110) surface exhibits *pmm* symmetry and the bcc Fe(110) is pseudohexagonal. Also on the Cu(110) surface [28], despite the scarce interaction between Cu and graphene, two possible domains, namely the R30° and R0° superstructures, can be formed, both characterized by a highly corrugated and highly periodical Moiré pattern.

Compared to graphene, in the case of h-BN the literature is more limited, and only recently have a few works dealing with the mechanistic understanding of the growth process emerged [10, 29]. Monolayer h-BN has been grown on the Pt(111) surface under UHV conditions using borazine [30], but the growth by chemical vapor deposition on Pt foils has also been investigated in order to prepare materials that could have a more direct application in technologically relevant fields. On the Pt(111) surface, h-BN forms a hexagonal (9×9) super-structure (i.e. matching ten unit cells of h-BN onto nine unit cells of Pt), which is characterized by a hexagonal Moiré [31] pattern whose origin is almost totally electronic; meanwhile, physical corrugation is very low. Alternative substrates investigated under high vacuum conditions are single crystals of Cu(111) [32, 33], Ni(111) [34–36], Ru(0001) [37, 38], Fe(110) [27], Pd(111) [39], Rh(111) [40], and Re(0001) [41], where the growth of monolayer h-BN has been studied by several techniques such as photoemission spectroscopy, STM, and electron microscopies. In particular, on pseudohexagonal bcc(110) surfaces, the growth of h-BN generally leads to the formation of a quite corrugated layer, as demonstrated by some works on Mo(110) [42], Cr(110) [43], and Fe(110) [27]. In this latter case, the h-BN layer is uniaxially strained and forms nanowaves with a periodicity of 2.6 nm and corrugation of 0.08 nm [27]. Notably, on the Pd(110) surface [44], h-BN grows while interacting very little with the noble metal surface, and therefore it can adopt several orientations; a complex mixture of different phases can be obtained, and among these a 'stripe-like' and a 'dot-like' superstructure are most frequent. However, on the Ni(110) surface, two different commensurate structures are formed, namely a (7×5) and a (1×6) [45], which are characterized by the presence of a modest strain and corrugation (up to 2.6%).

Methods

Experimental

Photoemission and diffraction measurements. Ultraviolet photoemission spectroscopy (UPS), x-ray photoemission spectroscopy (XPS), and low-energy electron diffraction (LEED) experiments were performed in a multitechnique UHV system operating at a base pressure of 3×10^{-10} mbar, equipped with an Omicron SPECTALEED Omicron and an

Escalab MKII VG analyzer. The XPS measurements were carried out using a twin anode soft x-ray source (Omicron DAR 400). The spectra were recorded in constant analyzer energy mode with a pass energy of 20 eV. Single UPS spectra were acquired at room temperature from the Γ to the K point of the Brillouin zone at steps of one degree of polar angle, using the He II emission line (40.8 eV) produced by an Omicron HIS 13 VUV photon source.

STM. STM measurements were acquired at room temperature in an UHV Multiscan Lab STM instrument from Omicron GmbH equipped with exchangeable piezo heads. The typical working pressure in the STM chamber was $<1 \times 10^{-10}$ mbar. Pt/Ir 90/10 tips were prepared by AC electrochemical etching in a saturated aqueous solution of $CaCl_2$ and cleaned before use in UHV by electron-induced heating. Tip biases and currents are in the range of ± 1.5 V and 0.1–32 nA, respectively.

For all the experiments, a clean and ordered (1×2)-Pt (110) surface was obtained after several cycles of Ar^+ sputtering, followed by a short exposure at 850 K to $\sim 10^7$ mbar of oxygen to eliminate a possible C contamination, and finally by annealing at 1000 K. The cleanness and crystallographic order of the Pt(110) were checked by LEED and XPS. At the end of the cleaning procedure, a sharp (1×2) reconstruction was observed.

Theoretical methods. The *ab initio* calculations exploit DFT, with GGA-PBE [46] exchange and correlation potential, and include van der Waals dispersion forces through DFT-D2 Grimme potential [47]. We adopt the formalism developed in the SIESTA code [48], which is based on the localized atomic orbital basis set and norm-conserving pseudo-potentials. We used a double zeta polarized basis set for all the species considered and an energy cutoff of 400 Ry. The atoms in the overlayer and in the outermost Pt layer were relaxed until the forces reached the cutoff of 0.04 eV Å^{-1}. STM simulations were performed with a Tersoff–Hamman approach [49], assuming a constant density of states for the tip. We consider the electronic density in an energy interval of 0.25 eV just below the Fermi level. We simulate a constant-distance STM image and apply a Gaussian spatial broadening of a 1 Å to the electronic density to mimic finite experimental resolution.

Results and discussion

Graphene on Pt(110)

In the present work, graphene was synthesized via the decomposition of ethylene (dosing at $\sim 2 \times 10^{-7}$ mbar, for 250 s, corresponding to 3.125 L) on the clean Pt(110) surface at 1000 K. At the end of the growth process, the sample was cooled down to room temperature in UHV using a 30 K min^{-1} rate. The full monolayer coverage was reached after 6 min
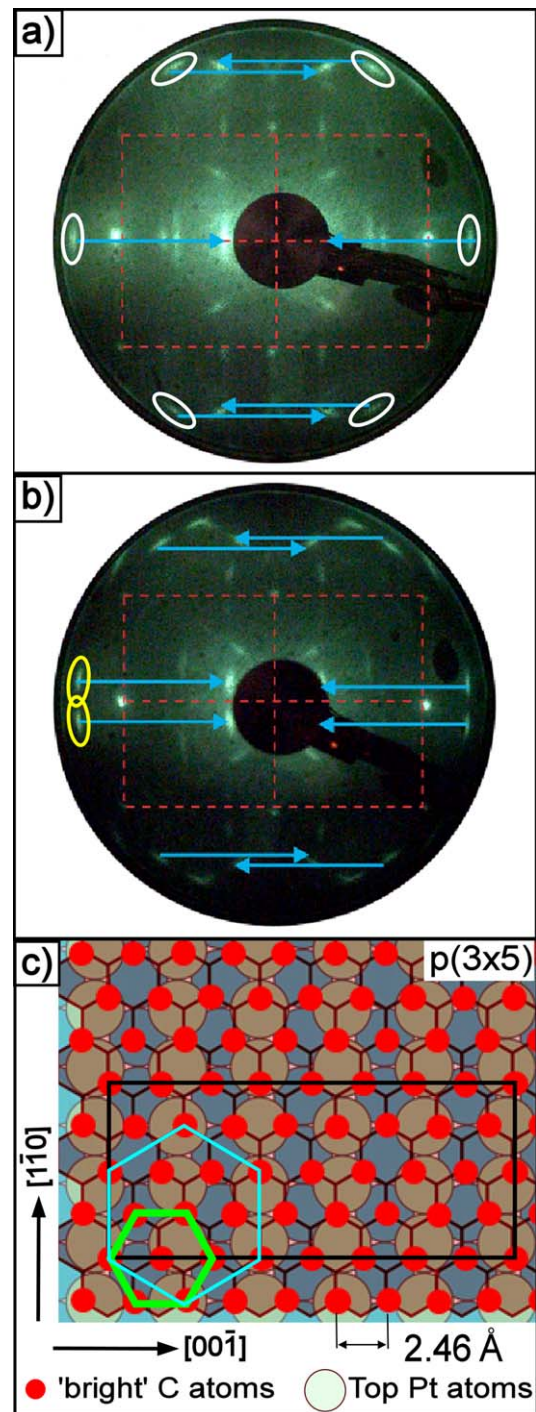

Figure 1. Panels (a) and (b) show LEED patterns (E = 50 eV) of graphene grown on Pt(110)-(1×2) for (a) nontilted domains and (b) $\pm 6°$ tilted domains, respectively. The red dashed line rectangle indicates the reciprocal cell of Pt(110)-(1×2); the light-blue arrows mark reflections of scattered graphene diffraction beams at the Pt interface. White ellipses in panel (a) mark graphene layer spots while yellow ellipses in panel (b) outline the further presence of the spots related to the tilted graphene domains. (c) Ball-and-stick model of nonrotated R0° graphene domains. Small green and large light-blue hexagons superimposed on the C lattice outline graphene super-structures observed in fast Fourier transform (FFT)–STM of the nontilted R0° graphene–Pt(110) layer in figure 2(b).
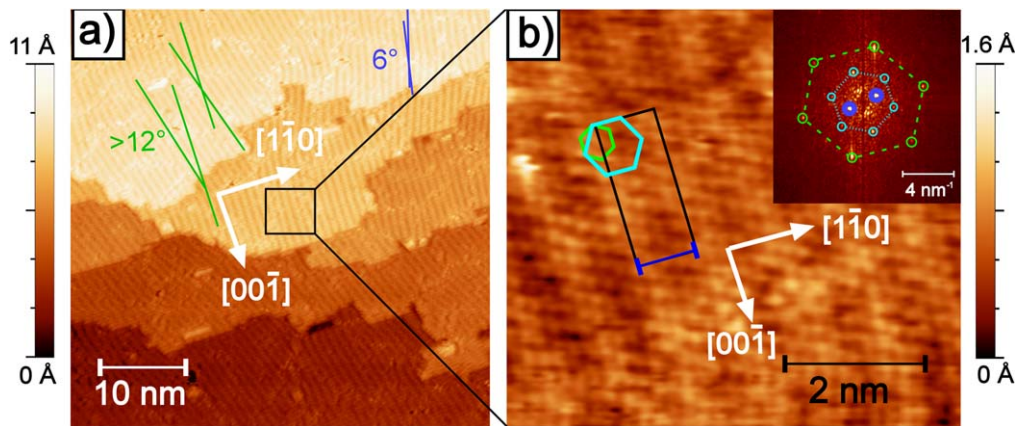
Figure 2. STM images of graphene grown on Pt(110) by the decomposition of C_2H_4 ($p = 1 \times 10^{-7}$ mbar, dose = 240 s), at full monolayer coverage: (a) ($V = -1.5$ V; $I = 0.3$ nA) at a wider scale different graphene rotational domains are observed and some are outlined by blue crossing lines (6° tilt between neighbor domains) and green lines (relative domain tilt larger than 12°). (b) ($V = -0.094$ V; $I = 20.88$ nA) High-resolution frame of a graphene domain oriented along the Pt[00$\bar{1}$]||C[11$\bar{2}$0] direction in figure 2(a). The black rectangle outlines the graphene supercell on the Pt(110) lattice. In the upper right inset of frame (b), the FFT of the STM image is shown. The green and light-blue hexagons are related to the observed structure of the film in the reciprocal FFT space; these structures are also highlighted with the same colors in the corresponding real-space STM contrast.

exposure to ethylene. The LEED patterns of the surfaces obtained after 6 min exposure to C_2H_4 are shown in figure 1(a). There are three types of superstructures that can be distinguished:

1. A single domain structure (figure 1(a)) where the [11$\bar{2}$0] direction of graphene is aligned with the Pt [00$\bar{1}$] direction;
2. A pattern comprising two domains rotated by 6° with respect to the [00$\bar{1}$] direction of the Pt(110) surface, marked in figure 1(b) with yellow ellipses and light-blue arrows;
3. A structure characterized by diffuse arch-like diffraction spots (LEED reported in the supporting information, available online at stacks.iop.org/NANO/29/485201/mmedia).

In addition to the hexagonal pattern expected by the (0001) plane of graphene (indicated by the six white-dotted ellipses in figure 1(a)), systematic extra spots can be observed. These features can be attributed to multiple scattering events. In fact, graphene primary diffraction beams are scattered at the interface with Pt so that the hexagonal diffraction pattern of graphene is replicated by any reciprocal vector of the Pt(110) surface (see the light-blue arrows in figure 1).

A similar multidomain structure (two domains rotated by $\pm13°$, and one domain aligned with the [00$\bar{1}$] direction) was observed in the case of the graphene/Ni(110) system [50, 51]. In this case, the formation of a specific structure was connected to small differences in the morphology of the substrate, i.e. to a graphoepitaxy effect. On the Pt(110) surface we found that the formation of differently rotated graphene superstructures does not depend on thermodynamic conditions (i.e. temperature and pressure) and it is observed during the same preparation on different areas of the sample; therefore, it seems related to the local morphology of the substrate. Furthermore, the multidomain structure does not present significant structural differences at high or low coverage. The LEED pattern

allows us to define the model structures of graphene/Pt(110), and the ball-and-stick model of the R0° graphene domain structure is presented in figure 1(c). As it may be seen, the lattice of graphene is very close to a (3 × 5) coincidence structure with the Pt(110) surface. This would require a very modest contraction of the graphene lattice: about 0.4% in the [00$\bar{1}$] direction and 2.3% along the [1$\bar{1}$0] direction.

In order to fully characterize the local atomic structure we carried out STM measurements (see figure 2), which confirm that after 6 min of ethylene dosing at $\sim$2 × 10^{-7} mbar, the Pt surface is fully covered by a continuous monolayer film. On the graphene layer however, there are some defects (the dark areas in figure 2(a)) that likely correspond to vacancy islands and clusters of C vacancies. Large-scale STM images (figure 2(a)) show the existence of several rotational domains (20 nm max width) characterized by a variety of orientations of their Moiré pattern with respect to the [00$\bar{1}$] substrate direction: beside the predicted 6° rotation (blue lines) a larger misorientation of adjacent domains can also be seen (green crossing lines). This observation is in agreement with the LEED data showing diffused spots and arch-like features around graphene diffraction spots, which is indicative of an azimuthal disorder of the layer. A higher magnification STM image of a graphene domain, oriented along the main Pt substrate directions, shows the atomic resolution of the C lattice: only the atoms belonging to one sublattice are visible, and they are reported in the ball-and stick sketch of figure 1(c) as 'bright' C atom sites.

The FFT of the STM image (inset of figure 2(b)) is very similar to the LEED pattern, confirming that the long-range aligned structure is preserved at the nanometer scale. In the FFT filtered image, two main features are recognized: one outlined by green circles and dashed lines, which refers to the primitive C lattice with a 2.46 Å pitch cell of graphene, and a smaller hexagon corresponding to the 3 × 3R30° supercell (light-blue circles and dotted lines). The STM image confirms that the graphene layer grows, aligning the [11$\bar{2}$0] 'zig-zag'

direction of graphene with the [00$\bar{1}$] direction of the substrate and the [10$\bar{1}$0] 'armchair' direction along the [1$\bar{1}$0] direction of the substrate. In the recent work by T Gao *et al* [19] the graphene layer was reported to align with the [11$\bar{2}$0] direction, that is 30° off with respect to the Pt [00$\bar{1}$] direction. This discrepancy can be due to the different methods employed for the film preparation (ambient pressure versus UHV chemical vapor deposition) and to analysis problems intrinsic to the *ex situ* characterization of polycrystalline metal foils.

The FFT of the STM image also outlines the contrast modulation of the overlayer along the [1$\bar{1}$0] substrate direction (blue circles inside the smaller hexagon) with a period of 8.7 Å, corresponding to three Pt substrate lattice spacings along the [1$\bar{1}$0] direction. However, on the perpendicular direction, no distinct periodicity can be identified. Therefore, the STM images are in good agreement with the (3 × 5) unit cell determined by the LEED data and considerations based on the introduction of minimum strain. In general, the film morphology that is observed on surfaces with symmetry other than hexagonal [26–28] is characterized by a long-range modulation of graphene apparent height that follows the physical corrugation of the substrate (i.e. the closely packed rows are aligned with the Moiré direction).

In the present case however, the graphene corrugation does not follow the expected morphology due to the missing row of the substrate along the [00$\bar{1}$] direction, thus suggesting that the reconstruction has been removed as a consequence of graphene deposition. This is confirmed by some STM images (such as that in figure 2(a)) where it is possible to observe on the terraces a faint contrast compatible with the rectangular unit cell of the (1 × 1) Pt(110) surface; this is also confirmed by the disappearance of the reflections in the (0,n/2) fractional positions in the LEED pattern.

In order to clarify whether the corrugation observed in the STM images is a morphological or electronic effect, we performed *ab initio* calculations and theoretical simulations of the STM images using the Tersoff–Hamman approach. We considered the surface unit cell reported in figure 1 in which a (2 × 8) graphene superstructure is matched on a (3 × 5) substrate supercell terminating with a (1 × 1) reconstruction. As mentioned before, the choice of a × 5 periodicity along the [00$\bar{1}$] direction is based on the very low strain (≃0.4%) necessary to epitaxially match eight units of graphene with five units of Pt along this direction. Such a commensurate supercell was already suggested by a previous work of Janin *et al* [52] on the basis of STM measurements.

The calculation gives an equilibrium average distance between graphene and the outermost surface layer equal to 2.4 Å.

Notably, the graphene–substrate distance is smaller than on Pt(111) and on other weakly interacting surfaces (around 3 Å), but is longer than in strongly interacting systems like Ni(111) (2.1 Å). The relaxed structure is reported in figures 3(a) and 3(b) (side and top view, respectively). We found that the interaction with the substrate induces a corrugation of the graphene sheet only along the [1$\bar{1}$10] direction, with a buckling of 0.6 Å as deduced by figure 3(c), in which the color gradient represents the deviation from the average
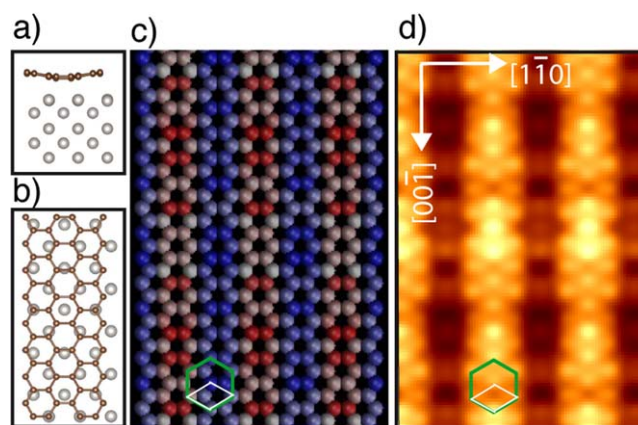

Figure 3. (a) Top and side view of the simulation cell. (b) Color gradient reproduces the deviation from the average distance (white): blue if longer, red if shorter. (c) STM simulation (details in the text). The graphene unit shell is shown in white while the green hexagon outlines the superstructure observed in the STM.

graphene–surface distance (blue larger, red smaller). Along the [00$\bar{1}$] direction of the substrate, the 'zig-zag' C lines are poorly corrugated and the maximum buckling amounts to 0.25 Å in the regions nearest to the substrate surface (blue in figure 3(c)). Therefore, the buckling seems to be the main mechanism for graphene to accommodate the mismatch with the Pt substrate. The topographic features of the STM images are reproduced by the contrast of our simulated STM image (figure 3(d)) and performed for a graphene–tip distance of approximately 2 Å. We verified that the same contrast is obtained considering empty and occupied states and different graphene–tip biases (lower than 1 V). The agreement with the measured STM is good within the limit of the experimental resolution, suggesting that the hypothesis of the lift of the surface reconstruction is reliable.

We also performed the calculations for graphene on the (1 × 2) surface reconstruction. In this case a substrate supercell with an even number of rows along the [00$\bar{1}$] is necessary to guarantee the periodicity. We chose a (3 × 8) supercell characterized by a small misfit with a (2 × 13) graphene supercell (i.e. 2.3%). The theoretical results relative to this configuration are reported in the Supporting Information. Notably, we found that the maximum corrugations along the [1$\bar{1}$10] (0.3 Å) and [100] (0.1 Å) direction are even smaller than in the previous case. The STM simulation for graphene on (1 × 2) Pt(110) is in qualitative agreement with the experiment regarding the brightness contrast. Thus, even if the highly corrugated Pt(100) (1 × 2) reconstruction was maintained, no sign of this morphological corrugation could be observed in the DFT calculations.

From the negligible corrugation of graphene and from the insensitivity to the morphology of the underlying surface, we can conclude that the interaction between graphene and Pt(110) is very weak. This is also confirmed by the interaction[5] energy

---

[5] The interaction energy is calculated as the difference between the energy of the overlayer on Pt(110) and that of the two separated systems in the relaxed configuration: $E_{int} = E_{G/hBN-Pt} - E_{G/hBN} - E_{Pt}$. The basis set superposition error (BSSE) correction has been included in the evaluation of this quantity.
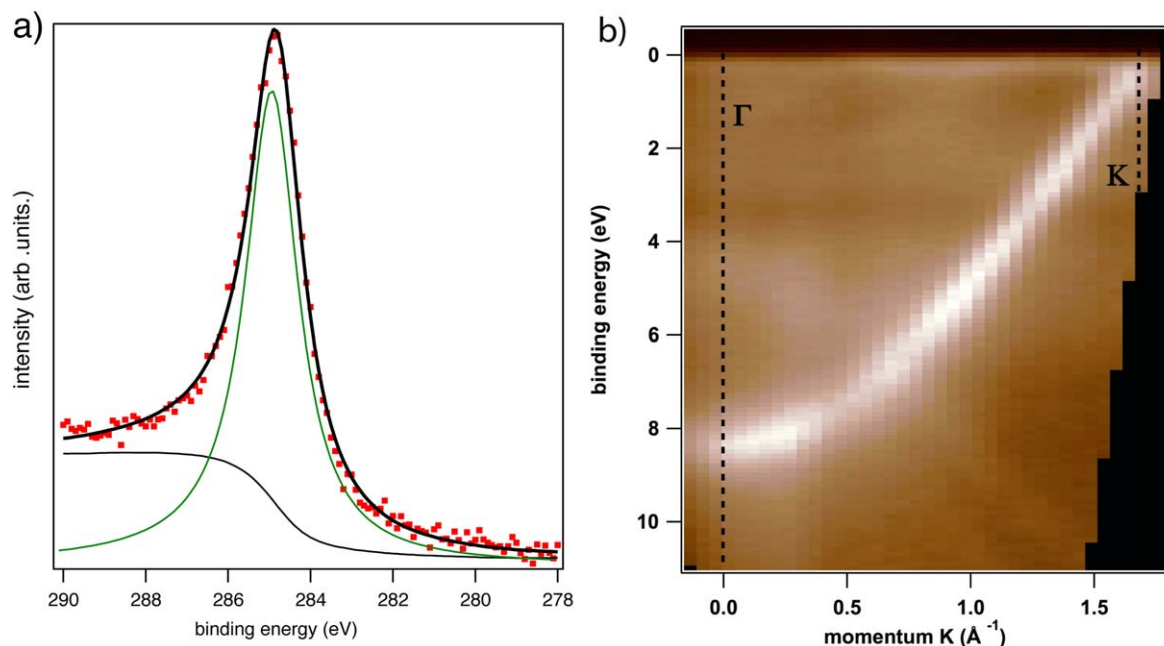
Figure 4. (a) C 1s photoemission peak for a fully covering graphene film on the Pt(110). (b) Angle-resolved valence band spectra acquired with He II exciting radiation (40.8 eV) from the $\overline{\Gamma}$ to the $\overline{K}$ point of the Brillouin zone for a fully covering graphene layer on Pt(110).

that amounts to -0.12 eV and is very similar to the adsorption energy[6] (-0.10 eV), thus indicating that there is a very small energy gain due to the graphene distortion.

The above discussion relative to the topographic effect, i.e. related to the atomic buckling, allows us to conclude that the different STM contrast observed along the two high-symmetry directions have to be ascribed *mainly* to a morphological effect, which is not a mere replica of the substrate corrugation.

Further evidence of the weak graphene–substrate interaction can be provided by XPS data both from the core levels and the valence band.

Figure 4(a) shows the C 1s photoemission line of a monolayer graphene film centered at 284.3 eV, as expected for C sp^2 atoms; it is slightly asymmetric and wider than the typical photoemission spectrum measured on freshly exfoliated, highly oriented pyrolytic graphite samples. The full width at half maximum is 1.3 eV, which is the same as that measured for identical experimental conditions on other metal substrates such as Pt(111). These results are in agreement with the previous data obtained by synchrotron radiation [52]. With the present spectral resolution no separated components associated with chemically distinct C atoms can be observed, but a unique Doniach-Sunjic peak is sufficient to reproduce the photoemission spectrum. This is at variance with the case of graphene layers on the Rh(111) and Ru(0001) surfaces, where highly corrugated films are formed as demonstrated both by STM measurements and by C 1s spectra where a clear doublet can be observed [16].

Moreover, in our case no changes are observed in the Pt 4f photoemission peaks before and after the deposition of the graphene film.

Additional information can be obtained by valence band spectra (figure 4(b)) where we can identify the presence of a very intense band crossing the $\overline{\Gamma}$ point at 8.2 eV, which can be associated with the π band of graphene. The σ band on the contrary is quite difficult to identify precisely, since it is much weaker and it overlaps with the Pt 5d band; however, it seems to be located in the $\overline{\Gamma}$ point at about 4.5 eV. Around the $\overline{K}$ point of graphene, it can be clearly seen that the π band exhibits a linear dispersion of E versus **k**, and the Dirac energy coincides with the Fermi energy, which excludes the presence of a significant charge transfer between the graphene layer and the support. This is in agreement with the theoretical values of the charge transfer derived from the analysis of the Mulliken charges. Altogether the spectroscopic data indicate the formation of a freestanding graphene layer poorly interacting with the underlying substrate. This situation is very similar to the case of the Pt(111) surface [23]. Therefore, the corrugated morphology and a low symmetry (*mmm*) of the Pt(110)surface do not affect the electronic properties of graphene, which are mainly determined by the weak chemical interaction between Pt and C.

h-BN on Pt(110)

In the present work, h-BN was grown on the (1×2)-Pt(110) reconstructed surface using the pyrolysis of the amino-borane complex, heated at 40 °C, and dosed through a leak valve on the substrate held at 1000 K. A partial pressure of 10^{-6} mbar and exposure time up to 30 min (corresponding to a dosing of 2.08 L) were necessary in order to obtain a fully covering

---

[6] The adsorption energy is calculated as the difference between the energy of the overlayer on Pt(110) and that of the two pristine (unrelaxed) systems: $E_{ads} = E_{G/hBN-Pt} - E^0_{G/hBN} - E^0_{Pt}$. The BSSE correction has been included in the evaluation of this quantity.
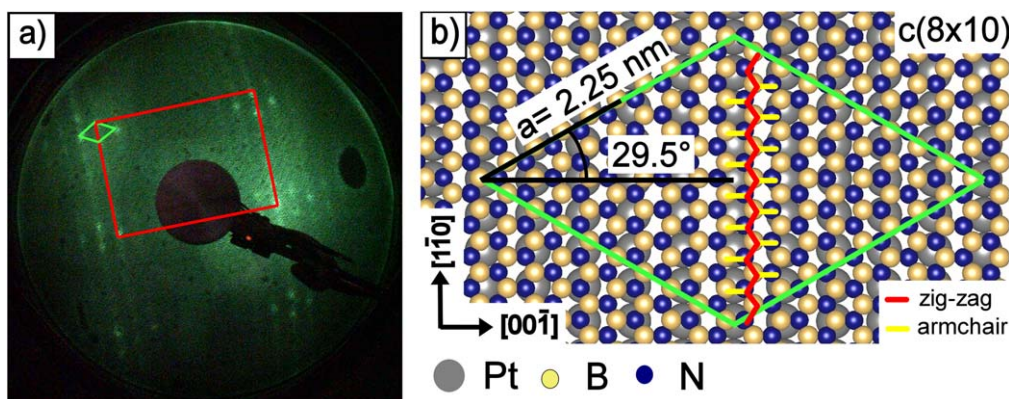
Figure 5. (a) LEED pattern of a fully covering h-BN/Pt(110) monolayer. The lattice cell of Pt(110) is outlined by the red rectangle and the h-BN lattice in light-green. (b) Ball-and-stick model of the h-BN/Pt(110) lattice cell. B, N, and Pt atoms are marked with blue, yellow, and light-gray circles, respectively. The h-BN cell with a 2.25 nm side is outlined in light-green. The angle between the h-BN cell and [00$\bar{1}$] direction is also shown (29.5°). The hexagonal lattice of h-BN has the 'armchair' direction along the [00$\bar{1}$] direction of the Pt substrate (yellow lines) while the 'zig-zag' one (red lines) runs along the [1$\bar{1}$0] direction of the substrate.

monolayer of h-BN. After the completion of one layer, the growth rate dramatically decreases, allowing a good control over single-layer films. This behavior can be easily understood considering the catalytic activity of Pt(110) toward dehydrogenation reactions and possible chemical interactions with NH_x and BH_x fragments compared with the relative chemical inertness of h-BN.

Figure 5(a) shows the LEED pattern of the fully covering h-BN layer on the Pt(110) surface, where a pattern corresponding to a c(8 × 10) superstructure can be clearly observed. It is worth noting that when the growth temperature is not sufficient (i.e. <1000 K) the diffraction pattern shows some distinct streaks running along the [00$\bar{1}$] direction. As will be discussed later, this indicates the possibility of the copresence of phases with slightly different periodicity.

Figure 5(b) shows the ball-and-stick model of the h-BN cell on the Pt(110) substrate, with a rhombic primitive cell with a 2.25 nm side, forming a 29.5° angle with respect to the [00$\bar{1}$] Pt substrate direction. Along the [00$\bar{1}$] direction, nine units of h-BN (4.34 × 9 = 39.06 Å) are matched over ten lattice units of Pt (3.92 × 10 = 39.2 Å). Along the [1$\bar{1}$0] direction nine units of h-BN (9 × 2.51 = 22.59 Å) are superimposed on eight units of Pt (2.77 × 8 = 22.16). According to this epitaxial relationship, the h-BN retains a negligible stress (<1%).

In this model the 'armchair' direction of the hexagonal BN lattice (yellow lines in figure 5(b)) is parallel to the [00$\bar{1}$] direction of the Pt substrate, while the 'zig-zag' edge (red lines in figure 5(b)) runs along the other main cell direction [1$\bar{1}$0]; therefore, these two directions are reversed with respect to the case of graphene on the same substrate.

Figure 6(a) shows a large-scale STM image of the h-BN film on the Pt(110) surface in which a striped pattern and a Moiré superstructure can be identified following a ×10 periodicity along the [00$\bar{1}$] direction; this is compatible with the LEED analysis. In particular, within a unit cell (blue line) in figures 6(b) and 6(c) eight lines can be identified and separated into two groups of four bright lines by a darker region. Notably, this number of lines does not match either with that

of the substrate (10) nor with that of the overlayer (9) in the observed c(8 × 10) commensurate superstructure. The ×10 periodicity is not respected in some regions of the sample, where a group of five lines instead of four can be identified, thus suggesting a larger periodicity; this finding is compatible with that for a ×12 periodicity. In fact, as shown in figure 6(b) in some c(8 × 10) patches, there are some systematic translational errors, and there are regions where some half-cells with c(8 × 12) periodicity are present. This local change of the periodicity leads to the formation of defects such as the shift along the [00$\bar{1}$] direction of the dark lines (see the arrows in figure 6(b)) that are distinctive of this structure.

The morphology of the h-BN film is shown in higher detail in figure 6(c). This image was acquired at tunneling current I = 2.85 nA and bias *V* = 61 mV.

The FFT of figure 6(c), reported in figure 6(d), matches with the LEED pattern in figure 5(a) and with the model of the h-BN overlayer proposed in figure 5(b).

In order to gain a deeper insight into the structural properties of the layer and how these are connected to the h-BN−Pt interaction, we performed *ab initio* DFT calculations considering the overlayer matched to a c(8 × 10) cell of Pt.

The overlayer stacking with respect to the substrate has been determined by a preliminary total energy calculation for a (1 × 1) supercell with B and N atoms in different high-symmetry positions: B on top, N on top, and Pt at the center of the h-BN hexagon. The N on top results in the most stable configuration with a h-BN-Pt distance of about 2.5 Å, which is in agreement with previous works related to h-BN on different transition metal surfaces [36, 53]. The geometry relaxation of the c(8 × 10) supercell gives a mean overlayer–substrate distance at equilibrium equal to 2.52 Å. The overall corrugation amounts to 0.5 Å, as can be deduced by figure 7(b), where the *z* coordinate of the B and N atoms is reported in a colorimetric scale indicating the overlayer–substrate distance relative to the average one.

The minimum overlayer–substrate distance is observed at the corners of the unit cell where N lies on top of a Pt atom.
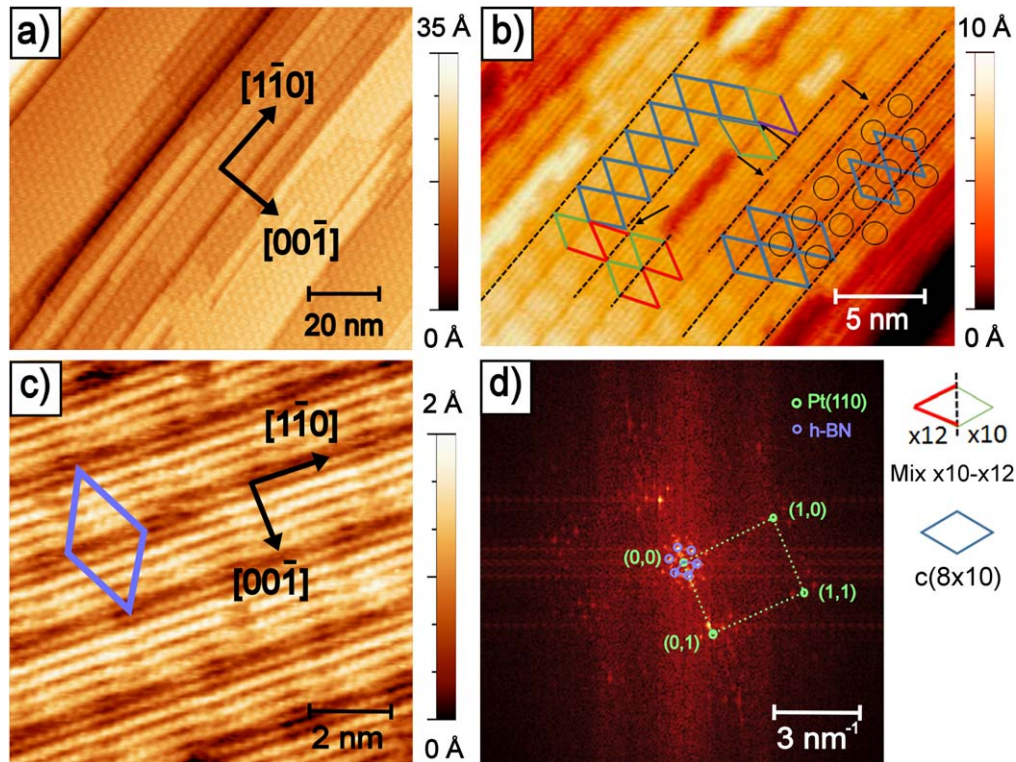
Figure 6. (a) Wide-scale STM view of h-BN/Pt(110) (V = −1.2 V; I = 1.58 nA). (b) A more detailed view of the h-BN/Pt(110) layer (V = −73 mV; I = 5.1 nA) showing different possible h-BN reconstructions coexisting on the Pt(110) surface, as also likely deduced from the streaked LEED pattern in figure 5(a): aside from the c(8 × 10) structure, outlined in light-blue lozenges, another possible (8 × 12) reconstruction, typically present only in half-cells and contiguous to the (8 × 10) reconstruction, is highlighted in red/green bicolor lozenges (mixed ×10−×12 supercell). The presence of this mixed phase induces line-stacking faults in the h-BN layer, indicated by black lines, and defect points indicated by the black arrows. (c) High-resolution STM frame (V = +61 mV; I = 2.85 nA) related to the h-BN empty states. The lattice cell of the h-BN film, shown in figure 5(b) is also highlighted here with a violet lozenge. (d) FFT–STM of panel (c), with the spots and substrate lattice vectors outlined in light-green (Pt) and violet (h-BN) circles.
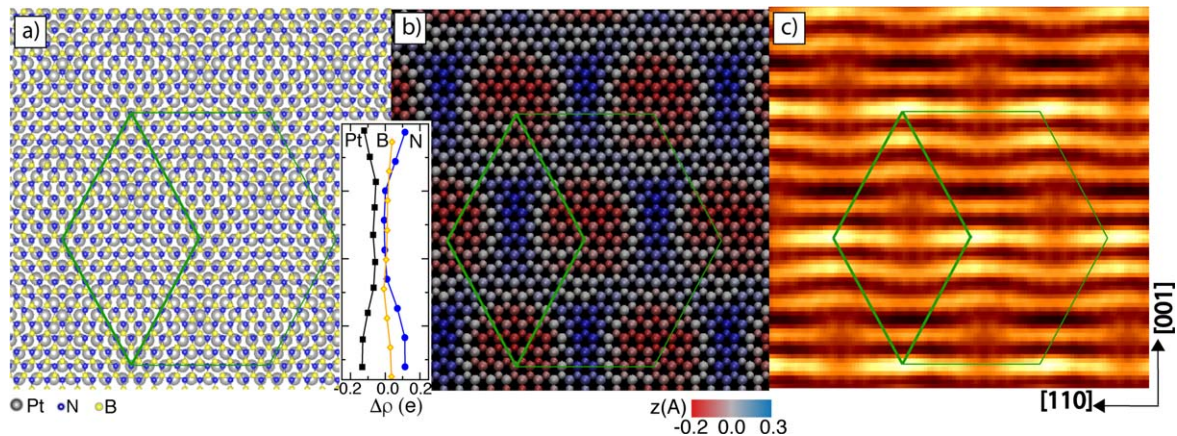

Figure 7. (a) Top view of the relaxed structure: Pt atoms are shown in gray while blue and yellow atoms corresponds to N and B, respectively. (b) Corrugation along *z*. The colorimetric scale shows the *z* displacement relative to the average h-BN–Pt distance (blue and red corresponding to larger and smaller distances with respect to the average value). (c) STM simulation at a distance of 2 Å from the overlayer. The inset shows the charge transfer along the diagonal of the supercell for Pt (black squares), B (yellow diamonds), and N (blue circles).

Differently, the central area of the unit cell is characterized by a higher *z* coordinate of h-BN that reaches its maximum when the N atom is in the middle of the Pt rectangular unit cell. However, on top B atoms generally lie at the mean equilibrium distance. The relationship between height modulation and N position relative to Pt allows us to infer that the chemical interaction with the substrate is driven mainly by the N–Pt interaction while B has a minor role. This is also confirmed by the charge transfer along the cell diagonal, which is plotted for the three species in the inset of figure 7 assuming as a reference the atomic valence charge in the freestanding h-BN overlayer and Pt surface, respectively. While the
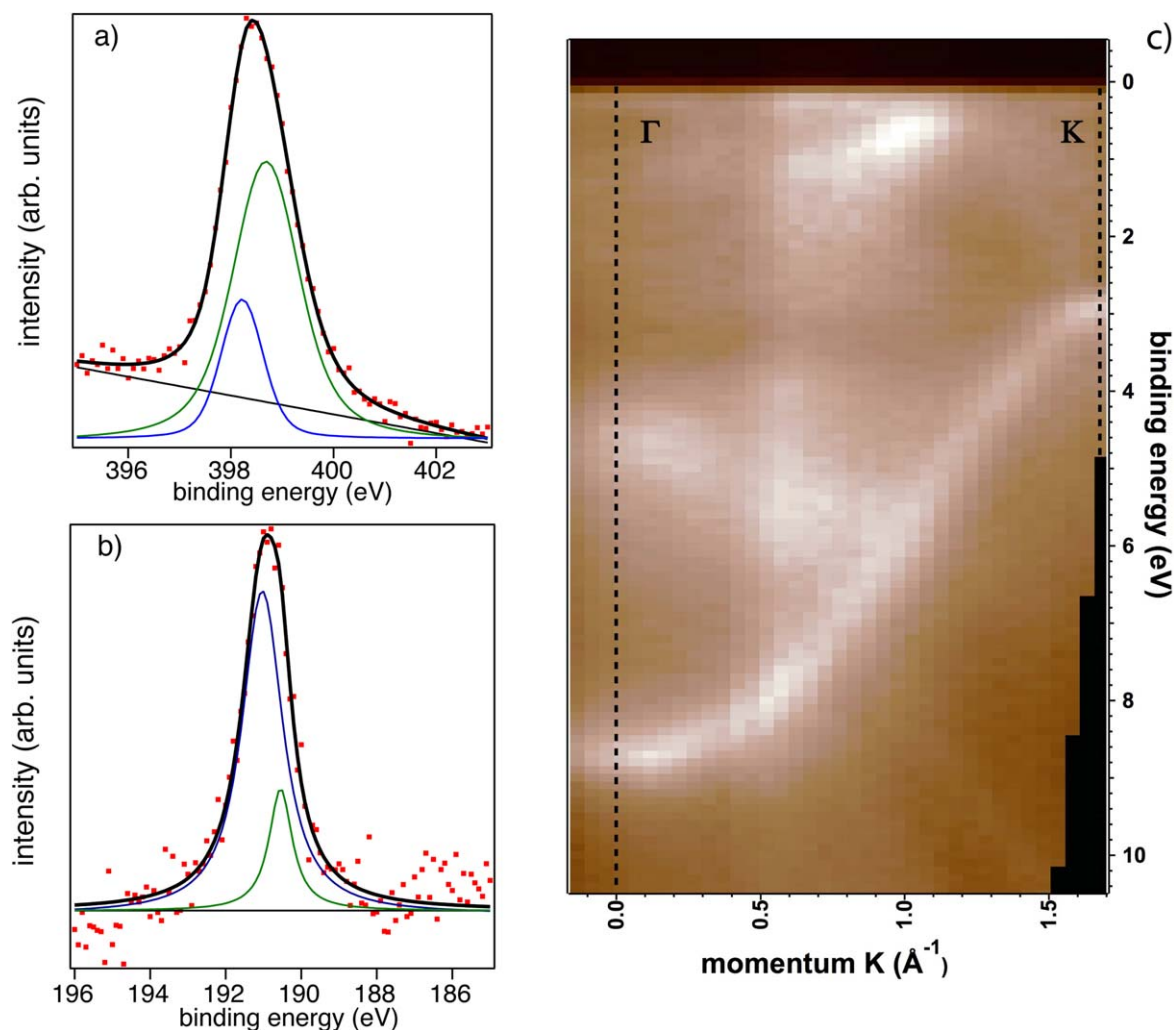
Figure 8. (a) B 1s photoemission peak for a fully covering h-BN film on the Pt(110). (b) N 1s photoemission peak for a fully covering h-BN film on the Pt(110). (c) Angle-resolved valence band spectra acquired with He II exciting radiation (40.8 eV) from the $\overline{\Gamma}$ to the $\overline{K}$ point of the Brillouin zone for a fully covering h-BN layer on Pt(110).

variation of B valence charge is negligible along the cell, Pt and N display a symmetric behavior along the diagonal with N acquiring charge from Pt when the former is on top of the latter. These observations suggest that, depending on the registry of the overlayer with respect to the substrate, different kinds of interaction between h-BN and Pt(110) can be present in the Moiré pattern, leading to electronic effects contributing to the observed STM spectra. Our STM simulation, reported in figure 7(c), shows both the Moiré superstructure and the eight bright lines found in the experimental images. While the former can be related to a morphological aspect due to the height modulation, the latter arises from the Pt–N proximity. From the joint analysis of the theoretical STM image and the structural properties in figures 7(a) and 7(b), we can deduce that the N atoms are imaged as a bright region in the STM; meanwhile, the B atoms give no contribution. Furthermore, we observe that moving along the cell diagonal, the N atoms in proximity of underlying Pt rows are responsible for the bright lines. Due to the change of registry along the cell, the final effect is that the bright lines are one less than the number of BN pairs in the cell, as explained in detail in the supporting

material. The STM simulation was obtained by integrating the charge density in an interval 0.25 eV wide just below the Fermi level and considering a tip–overlayer distance of 2 Å (we verified that the appearance of the theoretical image is poorly dependent on this distance).

We also performed the calculation for the (8×12) superstructure. The theoretical results, reported in the Supporting Information, are qualitatively very similar to those reported in figure 7 except for the different periodicity that give rise to ten lines in the unit cell instead of eight. Then our theoretical results confirm that the defective structure observed in figure 5(c) are due to a mixing of a c(8×10) and c(8×12) superstructure.

The calculated adsorption and interaction energies for this system are very similar ($E_{int} = -0.24$, $E_{ads} = -0.26$), suggesting that the effective interaction between the overlayer and the surface is weak.

The electronic properties of the h-BN layer were also investigated by XPS. Photoemission spectra from B 1s and N 1s core levels (figures 8(a), (b)) are centered respectively at 190.5 eV and 398 eV, which are the typical binding energies

for h-BN supported on metal substrates [30, 31, 54]. The N 1s spectrum can be fit by two components: a major one centered at 398.7 eV, which can be ascribed to the N atoms in perfect h-BN, and another one less intense at 398.2 eV, which can be probably associated with defects such as atoms located at grain boundaries and translational domains [55, 56]. The overall spectral fingerprint is very similar to what was observed in the same experimental conditions on h-BN on Pt(111), which is the paradigmatic case of a fully relaxed layer with no chemical interaction with the substrate. Similarly, in the B 1s photoemission line we can resolve two peaks: one at 191.0 eV and one at 190.5 eV, which can be associated with regularly coordinated and defective B atoms in h-BN.

The presence of a unique superstructure allowed us to acquire ARPES spectra from the valence band. In figure 8(c) we report the band dispersion from the $\overline{\Gamma}$ to the $\overline{K}$ point. It can be seen that the σ and π band cross the $\overline{\Gamma}$ point at 4.6 eV and 8.7 eV, respectively, which are almost the same values observed in the case of the Pt(111), Pd(111) [57], and Au/Ni (111) [54] surfaces. At the $\overline{K}$ point the π band reaches the valence band maximum, which is located at 2.9 eV. The body of photoemission data indicate that the h-BN layer is almost freestanding with a minimal electronic interaction with the Pt(110) surface.

Conclusions

In this work, we studied by using several techniques the structural and electronic properties of graphene and h-BN on a corrugated nonhexagonal metal substrate: the Pt(110) surface. In both cases, during growing conditions the Pt(110) (1 × 2) reconstructed surface is converted on a simple (1 × 1), which then is covered by the 2D atomic crystal. Despite the similar nature of the two materials, the subtle interplay between interaction energies, epitaxial constrains, and elastic properties leads to the formation of structurally different interfaces. Graphene can adopt several orientations with respect to the substrate, but the most favorable implies the alignment of the 'zig-zag' edge with the [00$\overline{1}$] direction of the Pt substrate. Conversely, the h-BN forms only one epitaxial structure that is characterized by the alignment of the 'zig-zag' edge with the [1$\overline{1}$0] direction of Pt. Interestingly, both materials interact very limitedly with the Pt surface and present the typical electronic features of noninteracting layers as demonstrated by photoemission measurements and by theoretical calculations. In more detail, the interaction between the 2D materials and Pt is essentially due to dispersion forces, and in the case of graphene it is extremely modest whereas in the case of h-BN it is more pronounced. In this latter case, it has been documented that the N atoms can accept a small amount of electron charge from the Pt substrate, whereas B atoms are essentially unaffected. The slightly enhanced interaction between h-BN and Pt accounts for the presence of a unique surface structure; being even less

interacting, graphene is free to adopt several azimuthally different orientations. The orthorhombic symmetry and intrinsic corrugation of the Pt(110) surface has only a small effect on both 2D materials. The graphene film is rather flat with a very small corrugation; similarly, the buckling in h-BN is very modest.

On the basis of our experimental and theoretical joint effort we can conclude that the Pt(110) substrate, despite the anisotropy of its clean surface, is a suitable template for the growth of quasi freestanding h-BN and graphene overlayers. The almost unaltered electronic properties and the negligible corrugation make these interfaces competitive with their most common analogous interfaces on Pt(111).

ORCID iDs

Simona Achilli https://orcid.org/0000-0001-6812-5043
Stefano Agnoli https://orcid.org/0000-0001-5204-5460

References

[1] Kuila T, Bose S, Mishra A K, Khanra P, Kim N and Lee J H 2012 *Prog. Mater. Sci.* **57** 1061–105
[2] Lyalin A, Nakayama A, Uosaki K and Taketsugu T 2013 *J. Phys. Chem.* C **117** 21359–70
[3] del Castillo E, Cargnoni F, Achilli S, Tantardini G F and Trioni M I 2015 *Surf. Sci.* **634** 62–7
[4] Banszerus L, Janssen H, Otto M, Epping A, Taniguchi T, Watanabe K, Beschoten B, Neumaier D and Stampfer C 2017 *2D Mater.* **4** 025030
[5] Lei S *et al* 2016 *Nat. Nanotechnol.* **11** 465
[6] Pagliara S, Tognolini S, Bignardi L, Galimberti G, Achilli S, Trioni M I, van Dorp W F, Ocelík V, Rudolf P and Parmigiani F 2015 *Phys. Rev.* B **91** 195440
[7] Tognolini S, Achilli S, Longetti L, Fava E, Mariani C, Trioni M I and Pagliara S 2015 *Phys. Rev. Lett.* **115** 046801
[8] Dedkov Y and Voloshina E 2015 *J. Phys.: Cond. Matter* **27** 303002
[9] Batzill M 2012 *Surf. Sci. Rep.* **67** 83–115
[10] Pakdel A, Bando Y and Golberg D 2014 *Chem. Soc. Rev.* **43** 934–59
[11] Reale F, Sharda K and Mattevi C 2016 *Appl. Mater. Today* **3** 11–22

[12] Li Q, Liu M, Zhang Y and Liu Z 2016 *Small* **12** 32–50

[13] Nappini S, Píš I, Menteş T O, Sala A, Cattelan M, Agnoli S, Bondino F and Magnano E 2016 *Adv. Funct. Mater.* **26** 1120

[14] Agnoli S and Granozzi G 2013 *Surf. Sci.* **609** 1–5

[15] Land T A, Michely T, Behm R J, Hemminger J C and Comsa G 1992 *J. Chem. Phys.* **97** 6774

[16] Preobrajenski A B, Ng M L, Vinogradov A S and MÅrtensson N 2008 *Phys. Rev.* B **78** 073401

[17] Gao T, Xie S, Gao Y, Liu M, Chen Y, Zhang Y and Liu Z 2011 *ACS Nano* **5** 9194

[18] Weatherup R S, Shahani A J, Wang Z, Mingard K, Pollard A J, Willinger M-G, Schloegl R, Voorhees P W and Hofmann S 2016 *Nano Lett.* **16** 6196–206

[19] Gao L *et al* 2012 *Nat. Commun.* **3** 699

[20] Choi J *et al* 2015 *ACS Nano* **9** 679

[21] Sutter P, Sadowski J T and Sutter E 2009 *Phys. Rev.* B **80** 245411

[22] Gao M, Pan Y, Huang L, Hu H, Zhang L Z, Guo H M, Du S X and Gao H 2011 *Appl. Phys. Lett.* **98** 033101

[23] Cattelan M *et al* 2015 *Nanoscale* **7** 2450

[24] Merino P, Švec M, Pinardi A L, Otero G and Martín-Gago J A 2011 *ACS Nano* **5** 5627–34

[25] Hwang J, Hwang H, Kim H, Ryu M-J, Lee J, Zhou Q, Mo S, Lee J, Lanzara A and Hwang C 2017 *Nanoscale* **9** 11498–503

[26] Politano A 2016 *Nano Res.* **9** 1795–800

[27] Vinogradov N A, Zakharov A A, Ng M L, Mikkelsen A, Lundgren E, Mrtensson N and Preobrajenski A B 2012 *Langmuir* **28** 1775–81

[28] Zhang J, Wang Z, Niu T, Wang S, Li Z and Chen W 2014 *Sci. Rep.* **4** 4431

[29] Zhang Z, Liu Y, Yang Y and Yakobson B I 2016 *Nano Lett.* **16** 1398–403

[30] Ćavar E, Westerström R, Mikkelsen A, Lundgren E, Vinogradov A S, Ng M L, Preobrajenski A B, Zakharov A A and MÅrtensson N 2008 *Surf. Sci.* **602** 1722

[31] Preobrajenski A B, Vinogradov A S, Ng M L, Ćavar E, Westerström R, Mikkelsen A, Lundgren E and MÅrtensson N 2007 *Phys. Rev.* B **75** 245412

[32] Joshi S *et al* 2012 *Nano Lett.* **12** 5821–8

[33] Preobrajenski A B, Vinogradov A S and MÅrtensson N 2018 *Surf. Sci.* **582** 21–30

[34] Auwärter W, Suter H U, Sachdev H and Greber T 2004 *Chem. Mater.* **16** 343–5

[35] Shi Y *et al* 2010 *Nano Lett.* **10** 4134–9

[36] Grad G B, Blaha P, Schwarz K, Auwärter W and Greber T 2003 *Phys. Rev.* B **68** 085404

[37] Brugger T, Günther S, Wang B, Dil J H, Bocquet M-L, Osterwalder J, Wintterlin J and Greber T 2009 *Phys. Rev.* B **79** 045407

[38] Goriachko A, He Y, Knapp M, Over H, Corso M, Brugger T, Berner S, Osterwalder J and Greber T 2007 *Langmuir* **23** 2928–31

[39] Morscher M, Corso M, Greber T and Osterwalder J 2006 *Surf. Sci.* **600** 3280–4

[40] Corso M, Auwärter W, Muntwiler M, Tamai A, Greber T and Osterwalder J 2004 *Science* **303** 217–20

[41] Qi Y, Zhang Z, Deng B, Zhou X, Li Q, Hong M, Li Y, Liu Z and Zhang Y 2017 *J. Am. Chem. Soc.* **139** 5849–56

[42] Allan M P, Berner S, Corso M, Greber T and Osterwalder J 2007 *Nanoscale Res. Lett.* **2** 94

[43] Müller F, Hüfner S and Sachdev H 2008 *Surf. Sci* **602** 3467

[44] Corso M, Greber T and Osterwalder J 2005 *Surf. Sci.* **577** L78

[45] Greber T, Brandenberger L, Corso M, Tamai A and Osterwalder J 2006 *e-J. Surf. Sci. Nanotech.* **4** 410

[46] Perdew J P, Burke K and Ernzerhof M 1996 *Phys. Rev. Lett.* **77** 3865

[47] Grimme S 2006 *J. Comput. Chem.* **27** 1787–99

[48] Soler J M, Artacho E, Gale J D, García A, Junquera J, Ordejón P and Sánchez-Portal D 2002 *J. Phys.: Condens. Matter* **14** 2745

[49] Tersoff J and Hamman D R 1985 *Phys. Rev.* B **31** 805

[50] Usachov D, Dobrotvorskii A M, Varykhalov A, Rader O, Gudat W, Shikin A M and Adamchuk V K 2008 *Phys. Rev.* B **78** 085403

[51] Fedorov A V, Varykhalov A, Dobrotvorskii A M, Chikina A G, Adamchuk V K and Usachov D Y 2011 *Phys. Solid State* **53** 1952

[52] Janin E, Göthelid M and Karlsson U O 2000 *Appl. Surf. Sci.* **162** 184

[53] Tonkikh A A, Voloshina E N, Werner P, Blumtritt H, Senkovskiy B, Güntherodt G, Parkin S S P and Dedkov Y S 2016 *Sci. Rep.* **6** 23547

[54] Usachov D, Adamchuk V K, Haberer D, Grüneis A, Sachdev H, Preobrajenski A B, Laubschat C and Vyalikh D V 2010 *Phys. Rev.* B **82** 075415

[55] Henk H, Pierucci D, Ben Aziza Z, Silly M G, Gil B, Sirotti F, Cassabois G and Ouerghi A 2017 *Appl. Phys. Lett.* **110** 023101

[56] Pierucci D *et al* 2018 *Appl. Phys. Lett.* **112** 253102

[57] Morscher M, Corso M, Greber T and Osterwalder J 2006 *Surf. Sci.* **600** 3280–4